UC Berkeley

UC Berkeley Previously Published Works

Title

Tandem Catalytic Antioxidant Nanoparticles Comprising Cerium Carbonate and Photoactive Metal Oxides

Permalink

https://escholarship.org/uc/item/63x6g52t

Journal

ACS Applied Nano Materials, 4(11)

ISSN

2574-0970

Authors

Mishra, Manish K
Callejas, Juan F
Pacholski, Michaeleen L
et al.

Publication Date

2021-11-26

DOI

10.1021/acsanm.1c02128

Peer reviewed

Tandem Catalytic Antioxidant Nanoparticles Comprising Cerium Carbonate and Photoactive Metal Oxides

Manish K. Mishra,[1] Juan Callejas,[2] Michaeleen Pacholski,[2] Jim Ciston,[3] Alexander Okrut,[1] Antony Van Dyk,[2] David Barton,[2] James C. Bohling,*[2] Alexander Katz*[1]

[1]Department of Chemical and Biomolecular Engineering, University of California, Berkeley 201 Gilman Hall, Berkeley, California, 94720-1462, United States

[2]Dow Chemical Company, Midland, Michigan 48674, United States

[3]National Center for Electron Microscopy Facility, Molecular Foundry, Lawrence Berkeley National Laboratory, Berkeley, California, 94720, United States

*correspondence to: askatz@berkeley.edu, JBohling@dow.com

ABSTRACT

While photoactive metal oxides such as TiO_2 find widespread use in society, e.g., as pigments in paints and coatings as well as UV filters in sunscreens and cosmetics, they also generate reactive oxygen species (ROS), which degrade materials and are associated with human-health pathologies. Here, we demonstrate a robust and potent antioxidant consisting of earth-abundant cerium carbonate nanoparticles as well as micron-size $Ce_2(CO_3)_3 \cdot 8H_2O$, which are characterized by powder X-ray diffraction and 4D STEM (scanning nanobeam diffraction). When dispersed with these same photoactive metal oxides, these cerium carbonate materials decrease the photodecomposition rate of organic dyes and commercial pigment-colorants in aqueous media by up to 820-fold, as well as in acrylic coatings. X-ray photoelectron spectroscopy and kinetics experiments support the same tandem-catalysis mechanism of photoprotection, when using both

micron-size $Ce_2(CO_3)_3 \cdot 8H_2O$ as well as cerium carbonate nanoparticles. This mechanism involves ROS disproportionation (catalyzed by cerium carbonate) and H_2O_2 decomposition (catalyzed by TiO_2) pathways, both of which cerium carbonate can also catalyze on its own, crudely mimicking the function of the cascade system of superoxide dismutase (SOD) and catalase enzymes. When cerium carbonate nanoparticles were dispersed at 2 wt. % in polymethylmethacrylate (PMMA), the transparency of the polymer film was preserved and photooxidative degradation of the polymer was prevented following UV irradiation, which otherwise resulted in loss of optical properties and hydroxylation according to ATR-FTIR spectroscopy, in the control poymer lacking cerium carbonate. Similar observations were made regarding color preservation in paint films comprising dye as well as insoluble commercial colorant pigments. The materials chemistry is subtle and emphasizes the importance of both Ce(III) and carbonate together, as both $CePO_4$ and Na_2CO_3 are inactive. This emphasis is also apparent in comparisons of photoprotection catalysis with previously reported cerium oxide nanoparticles, which are significantly less active (24-fold) compared with $Ce_2(CO_3)_3 \cdot 8H_2O$ under the same conditions.

1. INTRODUCTION

While high-refractive-index lead compounds were the white pigment of choice in paints and coatings since time immemorial, spanning hundreds of years, their use came to an abrupt stop in the United States in 1978, due to regulations concerning lead toxicity.[1,2] Their replacements consisting of metal-oxide pigment nanoparticles, such as TiO_2 and ZnO, have since been adopted in paints and coatings universally. TiO_2 and ZnO nanoparticles are also used as UV filters in sunscreens and cosmetics.[3] But their use has introduced a previously unforeseen challenge,

because these metal oxides are also photoactive, catalyzing the generation of reactive oxygen species (ROS) when exposed to light in the presence of water and O_2 .[4-11] These ROS have a profound deleterious effect on the environment, and are invoked in the degradation of natural ecosystems,[12] as well as materials that the paints and coatings are designed to protect in the first place.[13, 14] ROS have also been associated with several human pathologies, including neuronal loss observed in Alzheimer's disease,[15] premature aging ,[16-17] DNA damage[18] and skin cancer.[19, 20]

Because of this, photoactive metal-oxide pigments such as TiO_2 nanoparticles are typically surface-passivated (e.g., with a non-photoactive aluminosilicate overcoat).[21] However, while the surface passivation overcoat decreases ROS generation, significant amounts of leakage still occur,[21] and there thus continues to be a need for antioxidants that counteract photoactive metal oxides' production of ROS in all arenas that use them, including paints and coatings as well as personal-care products. Readily available organic antioxidants such as vitamins E and C, and green-tea leaf extract are sacrificial reductants and function stoichiometrically rather than catalytically, giving them generally low effectiveness against ROS.[22, 23] Nature uses catalysts that are based on enzyme cascades involving superoxide dismutase (SOD) and catalase, to decompose ROS in a tandem reaction that involves formation of hydrogen peroxide as an intermediate by SOD, which is subsequently transformed to water and O_2 by catalase.[17] However, employing these enzymes to decrease ROS concentrations in applications such as those alluded to above is highly impractical from both a cost as well as technical feasibility perspective, due to the general fragility of enzymes.

Here, we rely on the bad actor itself – the photoactive metal oxides that generate ROS such as TiO_2 – to demonstrate a tandem catalytic approach for highly potent antioxidants. This approach is inspired by the tandem catalytic function of SOD and catalase described above,[17] except now

translated to a synthetic materials platform. Our results demonstrate that when cerium carbonate nanoparticles are combined with the same photoactive metal oxides that catalyze ROS synthesis in the first place, the pair results in a robust tandem catalytic antioxidant, which consumes ROS before they can oxidatively degrade nearby organic molecules, at a rate and turnover number that is unrivaled by non-enzymatic systems. Our approach focuses on demonstrating proof of concept by using color retention of soluble dyes and insoluble commercial pigments in aqueous solution and paint coatings as a direct reporter that scales inversely with ROS concentration. Our manuscript separately demonstrates cerium carbonate nanoparticles to be highly active antioxidant catalysts for ROS degradation on their own, and extend these results to photostabilization of polymethylmethacrylate (PMMA), where we demonstrate preservation of transparency, as well as photostabilization of dye in aqueous solution.

2. RESULTS AND DISCUSSION

The active form of cerium carbonate can be synthesized in aqueous solution as micron-size particles, as well as nanoparticles in the average size range of 125 nm – 145 nm according to dynamic light scattering (DLS). These are efficiently synthesized upon rapidly mixing of two aqueous solutions, one of which consists of $(NH_4)_2Ce(III)(NO_3)_5 \cdot 4H_2O$, and the other $(NH_4)_2CO_3$, as shown in Figure 1a. This mixing results in precipitation of cerium carbonate as a product. Nanoparticles are obtained when this precipitation occurs in the presence of specific chelating organic ligands, as described below.

The powder X-ray diffraction (PXRD) pattern of the dried micron-size particles is shown in Figure 1b and exhibits a powder pattern comprising a prominent peak at approximately 10.3°

2θ, which is assigned to a crystalline micron-size $Ce_2(CO_3)_3 \cdot 8H_2O$ phase. This phase crystallizes

in an orthorhombic crystal structure (ICDD card no. 00-038-0377) with a = 0.8942 nm; b = 0.9529

nm; c = 1.6971 nm, and represents a layered material comprising stacked nanosheets, which

according to optical microscopy (using a differential interference contrast microscope) are 600 nm

thick and 5 – 10 μm in length in the wet state following synthesis (See Figurse S1a and S1b,

Supporting Information). Representative diffraction data from a 4D STEM[24,25] scan of micron-

size $Ce_2(CO_3)_3 \cdot 8H_2O$ are shown in Figure 1c, and the corresponding HAADF-STEM (high angle

annular dark field scanning transmission electron microscopy) image is shown in Figure 1d, with

the red box showing the area where the diffraction data of Figure 1c was collected. This imaging

technique is particularly amenable to cerium carbonate because of the short (1 – 10 ms) dwell

times and low electron dosages (300 electrons/Å^2 – about 2 orders of magnitude lower than

conventional STEM), which obviate beam damage, as carbonates are generally known to be highly

fragile under the beam. We compared k and h measurements from 4D STEM in Figure 1c with the

expected (020) and (200) distances from PXRD in Figure 1b, respectively (k = 0.454 nm versus

PXRD (020) = 0.476 nm; h = 0.406 nm versus PXRD (200) = 0.447 nm; k/h ratio = 1.12 versus

PXRD (020)/(200) ratio = 1.06). We attribute the slightly smaller (0.2 – 0.4 Å) distances measured

by 4D STEM relative to PXRD to be the result of unit cell contraction accompanying water loss

under the high vacuum of the electron microscope. The angle between the (020) and (200)

directions is measured to be 89.9 degrees by 4D STEM, which is close to the 90 degrees measured

by PXRD for this orthorhomic phase. These measurements cannot be the result of beam damage

to cerium carbonate, which in our hands results in cerium oxide synthesis under the beam, because

even the largest d-spacing in cerium oxide is too small to account for our 4D STEM data (i.e. this

distance is 0.31 nm along the (111) direction in cerium oxide[26]). The layers comprising these

particles are shown from the refined crystal structure for $Ce_2(CO_3)_3 \cdot 8H_2O$ in a side (h-l plane) and top (h-k plane) view in Figure 1a. The morphology evident from the STEM images in Figure 1d is consistent with the layered morphology from the plate-like appearance of the particles, in which their h-k planes are exposed perpendicular to the direction of the microscope beam, which penetrates along the c axis. These planes form nanosheets that bond with each other only through non-covalent interactions such as hydrogen bonding involving waters located in between nanosheets – not covalent interactions. The diffuse-reflectance UV-Vis (DR-UV-Vis) spectrum of this material has sharp absorption bands at 240 nm, 252 nm, and 272 nm, which are assigned to Ce(III) sites (see Figure S1c; Supporting Information), and the ATR-FTIR spectrum exhibits distinct bands at 1339 cm^{-1}, 1368 cm^{-1}, and 1468 cm^{-1}, corresponding to strongly coordinated carbonate anions (see Figure. SS1d; Supporting Information).
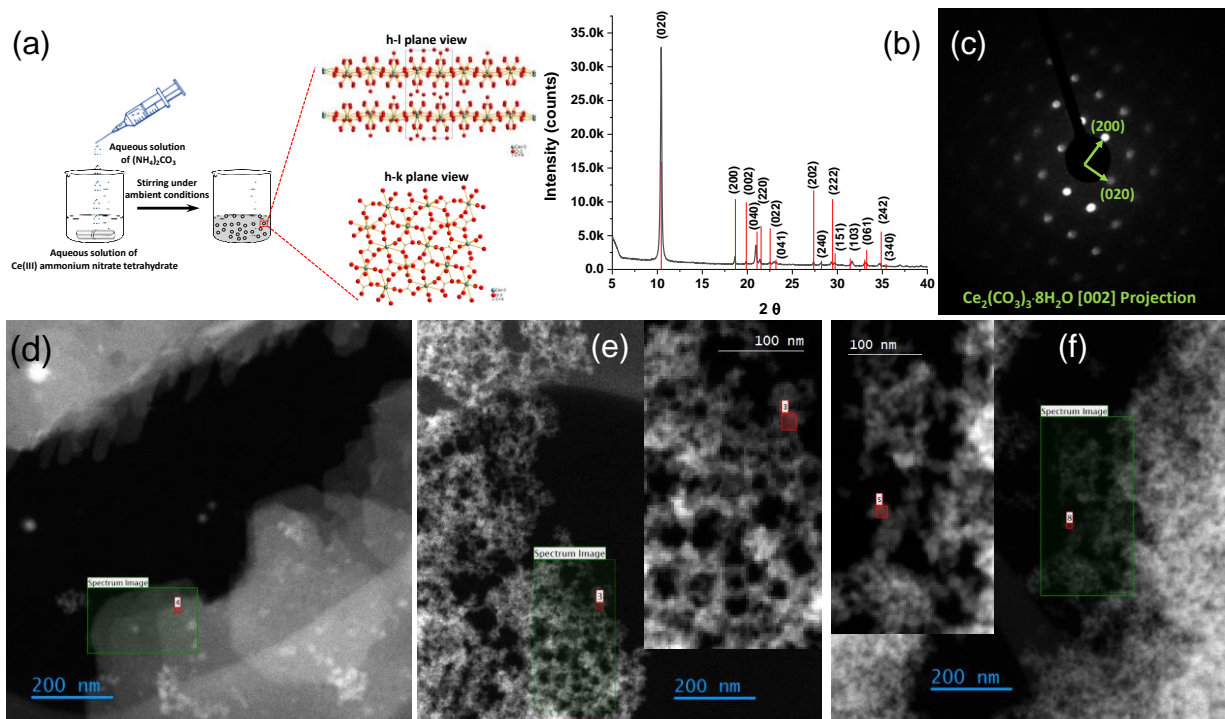
Figure 1. (a) Schematic of micron-size $Ce_2(CO_3)_3 \cdot 8H_2O$ synthesis, (b) PXRD pattern of micron-size $Ce_2(CO_3)_3 \cdot 8H_2O$ with major crystalline planes indexed, (c) representative electron diffraction data from 4D-STEM imaging of micron-size $Ce_2(CO_3)_3 \cdot 8H_2O$, (d) Overview 4D-STEM image of micron-size $Ce_2(CO_3)_3 \cdot 8H_2O$, with red box showing region where diffraction pattern in (c) was collected, (e) Overview 4D-STEM image of EDTA-capped cerium carbonate nanoparticles, with inset on right showing magnified view of image corresponding to green box in main figure, (f) Overview 4D-STEM image of NTA-capped cerium carbonate nanoparticles, with inset on left showing magnified view of image corresponding to green box in main figure.

We also synthesized $Ce_2(CO_3)_3 \cdot 8H_2O$ nanoparticles in order to achieve optical transparency in suspension, by conducting a similar one-pot synthesis to the one shown in Figure

1a, except in the presence of various chelating organic ligands. Among the several organic ligands investigated (see Table S2, Supporting Information), ethylenediamineteraacetic acid (EDTA), nitrilotriacetic acid (NTA) and polyacrylic acid (PAA) resulted in stable nanoparticles, which could be dispersed in water and afforded particle sizes in the average size range of 117 – 140 nm according to DLS data (see Figure S2a-c, Supporting Information). The first two of these exhibit the best performance as catalytic antioxidants (*vide infra*), and we characterized them both by 4D STEM, as shown in Figures 1e (EDTA-capped cerium carbonate) and 1f (NTA-capped cerium carbonate). They both consist of small primary particles (less than 10 nm in particle size) aggregated into larger secondary lacey structures, which we surmise are the ones detected by dynamic light-scattering in aqueous dispersions (*vide supra*; see Figure S2, Supporting Information). Electron diffraction collected of sample located in the red box in Figures 1e and 1f resulted in amorphous patterns for the latter two cerium carbonate nanoparticles (see Figure S2, Supporting Information). While the bulk PXRD data for EDTA-capped cerium carbonate nanoparticles exhibit intensity corresponding to the same prominent 10.3° 2θ peak as observed in Figure 1c for micron-size $Ce_2(CO_3)_3 \cdot 8H_2O$ above (assigned to (002)) (see Figure S2d; Supporting Information), we infer that most of this material is amorphous. We observe the same strongly bound carbonate bands by ATR-FTIR spectroscopy at 1368 cm^{-1} and 1468 cm^{-1} (See Figure S2e, S2f; Supporting Information) and the same Ce(III) bands by DR-UV-Vis for the EDTA-capped nanoparticles as we observed for the larger, micron-size cerium carbonate described above (see Figure S1c, S1d; Supporting Information). We conclude that the EDTA-capped cerium carbonate nanoparticles comprise the same chemical species as found in the micron-size sample.

For the NTA-capped cerium carbonate nanoaprticles, the surface chemical composition investigated by XPS (See Figure S3a; Supporting Information) exhibits a similar Ce to CO_3^{2-} ratio

of 0.68, which we also observed for micron-size $Ce_2(CO_3)_3 \cdot 8H_2O$ (*vide infra*). In addition, the UV-visible spectra (see Figure S3b; Supporting Information) of these two materials showed similar absorption bands. We therefore conclude that the NTA-capped cerium carbonate nanoparticles also comprise the same chemical species as found in the micron-size sample. We make a similar conclusion for the polyacrylic acid-capped cerium carbonate nanoparticles, based on DR-UV-visible spectroscopy (see Figure S3c; Supporting Information). No PXRD intensity was detected for the NTA-capped and polyacrylic acid-capped nanoparticles (see Figure 3d, Supporting Information), leading us to conclude those nanoparticles were amorphous.

We first investigated the function of micron-size $Ce_2(CO_3)_3 \cdot 8H_2O$ and P25 TiO_2, the latter on its own well known to be a highly active ROS photogenerator,[26] as tandem antioxidants in aqueous dispersion. In the absence of micron-size $Ce_2(CO_3)_3 \cdot 8H_2O$, when only the P25 TiO_2 (2 mg/100 mL; Degussa) is dispersed in an aqueous solution of MB dye as a control, spectra in Figure 2a demonstrate 98% dye photodegradation following 6 min of UV irradiation (corresponding to a pseudo-first-order rate constant for dye degradation of 0.65 min^{-1}). However, when the same experiment is instead conducted in a dispersion containing both micron-size $Ce_2(CO_3)_3 \cdot 8H_2O$ (1 mg/100 mL) in addition to the same amount of P25 TiO_2, we observe a 650-fold decrease in the initial rate constant for MB dye photodegradation in Figure 2c (k = 1 $x10^{-3}$ min^{-1}). Data shown in Figure 2 (e, f) and Figure S4 (Supporting Information) demonstrate similarly dramatic photostabilization effects when pairing EDTA-capped and NTA-capped cerium carbonate nanoparticles and P25 TiO_2 (see Figure 2 (g-i) and Figure S5, Supporting Information). As summarized in Table 1, these exhibit an 818-fold (EDTA-capped) and 1625-fold (NTA-capped) lower initial rate constant for MB dye photodegradation, respectively, compared to a control comprising the TiO_2 aloneFor polyacrylic acid-capped nanoparticles, we observe a slightly lower

photostabilization effect compared to the other cerium carbonate nanoparticles, corresponding to an initial rate constant of k = 1x 10^{-3} min^{-1} (see Figure2 (i, j)). On this basis, we focused the remainder of our attention in this manuscript on the EDTA-capped and NTA-capped cerium carbonate nanoparticles.

To investigate whether the results above in photostabilizing dye during photocatalytic degradation were independent of the particular dye molecule chosen as a reporter, we also conducted experiments with Rhodamine B (RhB) dye, and these results are also summarized in Table 1 (see Figs. S6a-f, Supporting Information). They demonstrate at least a 724-fold decrease in the rate of RhB photodegradation in similar experiments that pair micron-size $Ce_2(CO_3)_3 \cdot 8H_2O$ and EDTA-capped nanoparticles and P25 TiO_2. Tandem antioxidant photoprotection is also observed with insoluble organic-dye pigments (organic red and phthalo blue), which are used in commercial coating formulations (see Figure S7a-d, Supporting Information) when using the micron-size cerium carbonate. These latter results emphasize that interactions between the dye and the cerium carbonate and TiO_2 are not required for catalytic photoprotection function. Based on the data above all together, we conclude that the observed tandem antioxidant activity of cerium carbonate and TiO_2 is independent of dye structure.
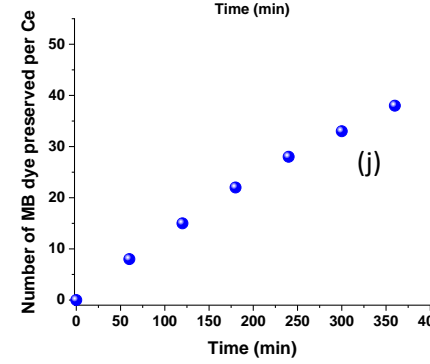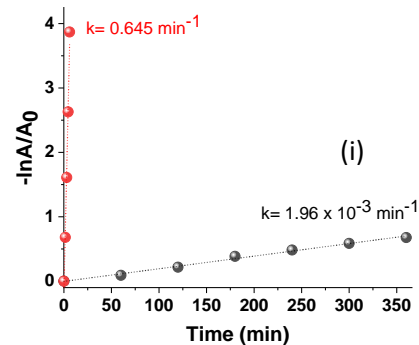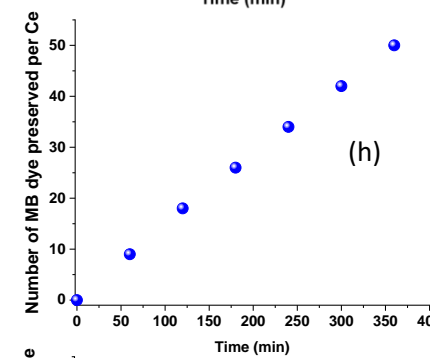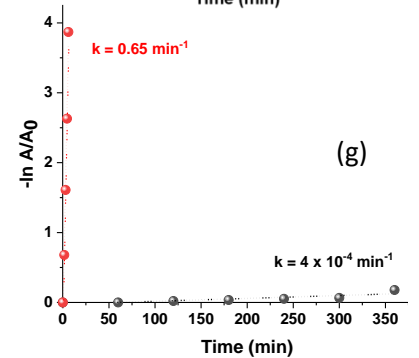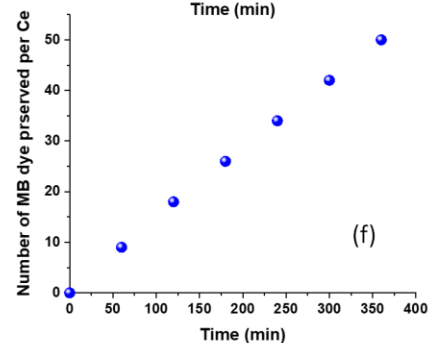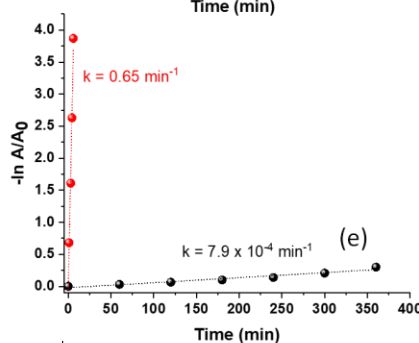
Figure 2. UV-visible spectra characterizing photodegradation of 100 mL of methylene blue solution (10^{-5} M) in presence of (a) P25 TiO_2 (2.5 x10^{-5} mol; 2 mg), (b) P25 TiO_2 (2.5 x10^{-5} mol; 2 mg) and micron-size $Ce_2(CO_3)_3 \cdot 8H_2O$ (2.1 x 10^{-6} mol; 1 mg), (c) pseudo-first-order rate constant of MB dye degradation in absence of micron-s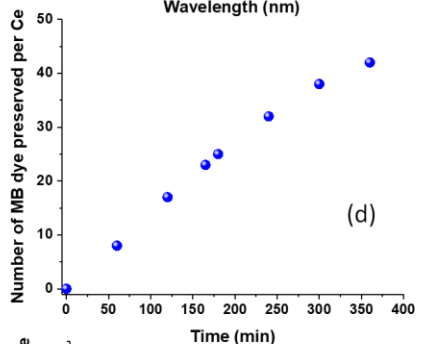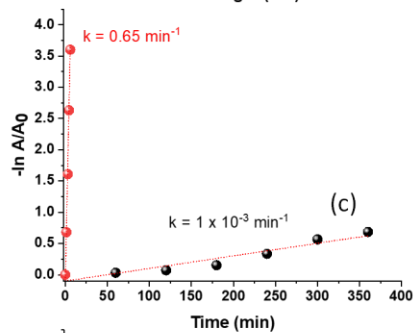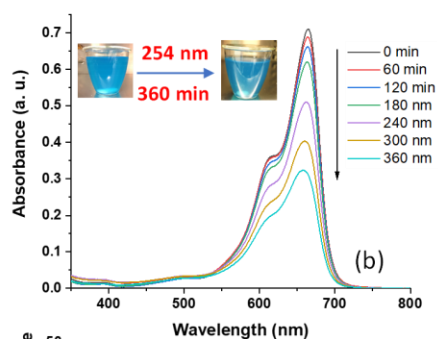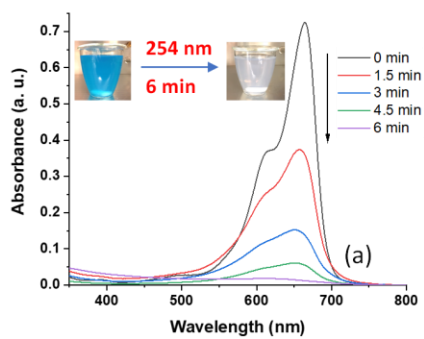ize $Ce_2(CO_3)_3 \cdot 8H_2O$ (red) and presence of micron-size $Ce_2(CO_3)_3 \cdot 8H_2O$ (black), (d) number of MB dye molecules protected by per Ce-atom based on data in (c), (e) pseudo-first-order rate constant of similar MB dye degradation experiments in presence (black) and absence (red) of EDTA-capped cerium carbonate nanoparticles (1 mg), and (f) number of MB dye molecules protected per Ce atom based on data in (e), (g) pseudo-first-order rate constant of MB dye degradation in absence of antioxidant additive (red) and presence of NTA-capped cerium carbonate (black), (h) number of MB dye molecules protected by per Ce-atom based on data in (g), (i) pseudo-first-order rate constant of MB dye degradation in absence of antioxidant additive (red) and presence of PAA-capped cerium carbonate (black), and (j) number of MB dye molecules protected by per Ce-atom based on data in (h).

Table 1. Summary of pseudo-first-rate constant for MB dye degradation in an aqueous slurry containing P25 TiO$_2$ photocatalyst as a control, and a mixture of the P25 TiO$_2$ and various cerium carbonates including micron-size Ce$_2$(CO$_3$)$_3$·8H$_2$O and cerium carbonate nanoparticles. N/A means data not available.

Additive	Initial pseudo-first-order rate constant of MB dye photodegradation (min^{-1})	Initial pseudo-first-order rate constant of RhB dye photodegradation (min^{-1})	Number of dye molecule preserved during 6 h photocatalysis
None (control)	k = 0.65 ± 0.04	k = 0.25 ± 0.02	0
Ce$_2$(CO$_3$)$_3$·8H$_2$O (CeC)	k = 1.0 x 10^{-3} ± 2.1 x10^{-5}	k = 3.4 x 10^{-4} ± 7.6 x 10^{-5}	42
EDTA-capped CeC	k = 7.9 x 10^{-4} ± 6.9 x 10^{-5}	k = 9.7 x 10^{-4} ± 7.84 x 10^{-5}	50
NTA-capped CeC	k = 4 x 10^{-4} ± 9 x 10^{-5}	N/A	50
PAA-capped CeC	k = 1 x 10^{-3}	N/A	38

We address the question of catalytic versus stoichiometric photoprotection with a combination of micron-size Ce$_2$(CO$_3$)$_3$·8H$_2$O and P25 TiO$_2$ by examining the number of MB dye molecules preserved per total Ce atom during the 6 h photocatalysis experiment (see section S1.9, Supporting Information) in Figure 2d. These data demonstrate that a total of 42 MB dye molecules were preserved per total Ce atom for the 6 h duration of the experiment. Based on this, we conclude that multiple turnovers of MB-dye photoprotection by the micron-size Ce$_2$(CO$_3$)$_3$·8H$_2$O were observed. Similar data were recorded for RhB (see Figure S6, Supporting Information). Using the same 6 h photocatalysis experiment with MB dye, we also characterized the EDTA-capped, NTA-capped, and polyacrylic acid-capped cerium carbonate nanoparticles, and results are shown in Figure 2. These data demonstrate a total of 50 MB dye molecules preserved per total Ce atom in

the EDTA- and NTA-capped nanoparticles, and this number was slightly lower (38) for the polyacrylic acid-capped nanoparticles. Altogether, these data support a catalytic mechanism of photoprotection involving cerium carbonate and P25 TiO_2.

These catalytic photoprotecting effects differentiate cerium carbonate from sacrificial reductants such as vitamin E, which are known to be irreversibly consumed upon reaction with a ROS into a less reactive, oxidized product, and as such, preserve less than a single dye molecule per molecule of photoprotecting agent (see Figure S8, Supporting Information).[22] Similar experiments involving cerium oxide nanoparticles dispersed in an aqueous organic-dye suspension containing TiO_2 photocatalyst have been previously reported;[27, 28] however, in these instances, the total number of dye molecules preserved per total Ce atom is between 0.4 – 1.9 (see Table S3, Supporting Information). When comparing a commercial cerium oxide nanoparticulate photostabilizing agent (Rhodigard® W185, Solvay) as well as a commercial zinc oxide (NANOBYK-3860) with micron-size $Ce_2(CO_3)_3 \cdot 8H_2O$, the latter was 24-fold (compared with cerium oxide) and 59-fold more effective (compared with zinc oxide) at photoprotecting an aqueous MB suspension (see Figure S9, Supporting Information). This stark difference underlines the greater effectiveness of a combination of cerium carbonate and P25 TiO_2 as a tandem catalytic antioxidant over cerium oxide and P25 TiO_2, besides the other advantages of cerium carbonate over cerium oxide such as redox stability in aqueous suspension[29] and chemical stability in presence of reducing organic compounds (see Figure S10 (a, b), Supporting Information). We also compared photoprotection catalysis under similar conditions with commercial hindered amine light stabilizers (HALS), which is an important class of organic based antioxidant, and our results demonstrate a sub-stoichiometric nature of photoprotection, differentiating HALS from the tandem catalytic antioxidant cerium carbonate/TiO_2, which also has a more than 33-fold lower rate

constant for aqueous dye photodegradation under similar conditions (see Figs. S11 and S12, and Table S4, Supporting Information).

We characterized the surface states of micron-size $Ce_2(CO_3)_3 \cdot 8H_2O$ using X-ray photoelectron spectroscopy (XPS) in fresh and used micron-size $Ce_2(CO_3)_3 \cdot 8H_2O$ (antioxidant catalyst was collected after 0.5 h, 1 h, and 2 h of MB dye photodegradation under the same reaction conditions as used in Figure 2b). A control was prepared by mixing fresh micron-size $Ce_2(CO_3)_3 \cdot 8H_2O$ sample in an aqueous MB dye dispersion containing P25 TiO_2, in the dark for 0.5 h. The Ce 3d XPS spectrum of this control sample is shown in Figure 3a, and exhibits Ce(III) peaks at 886 eV (strong) and 905 eV (strong) and no evidence of Ce(IV). The Ce 3d XPS spectra of all used micron-size $Ce_2(CO_3)_3 \cdot 8H_2O$ antioxidant catalyst samples are shown in Figure 3b. These exhibited the same Ce(III) peaks as above, in addition to peaks corresponding to Ce(IV) at 883 eV, 889 eV, 898 eV, 901 eV, 908 eV, and 917 eV (strong). We utilized this latter peak (its total area normalized to high-energy background at 925 eV) as a quantitative measure of surface-site transformation to Ce(IV) during photoprotection catalysis, and this peak area is represented in Figure 3c for the first 2 h of photoprotection catalysis. Data in Figure 3c demonstrate the onset of a steady state in the normalized 917 eV peak area for used antioxidant catalysts comprising 30 min – 2 h of photoprotection catalysis. We conclude that some transformation of initially Ce(III) sites in the fresh antioxidant catalyst to Ce(IV) occurs near the surface during photoprotection catalysis, and that a steady state was established, which we surmise represents interconversion between the two valence states, i.e. a Ce(III)/Ce(IV) redox couple occurs at the surface during photoprotection catalysis. Similar data on used photoprotection catalysts were obtained using the NTA-capped cerium carbonate nanoparticles (Figure S3a; Supporting Information). These data showed that after initial conversion of some surface Ce(III) to Ce(IV), a steady state in the normalized 917 eV

peak area (Ce(IV)) was obtained for the first 4 h of photoprotection catalysis, which confirms the rapid interconversion between the two valence states during photoprotection catalysis for the NTA-capped nanoparticles.

We also investigated the C1s XPS spectra (see Figure S13, Supporting Information) of all used micron-size $Ce_2(CO_3)_3 \cdot 8H_2O$ samples including the control. The average surface ratio of $Ce:CO_3^{2-}$ obtained from these C1s spectra is 0.67 (see Table S5, Supporting Information), and corresponds to the ratio that is predicted by stoichiometry for micron-size $Ce_2(CO_3)_3 \cdot 8H_2O$. We conclude that the surface composition of Ce and CO_3^{2-} reflects the bulk and that photoprotection catalysis does not change this surface composition. When this result is combined with the aqueous insolubility of cerium carbonate (i.e. it is the predominant form of cerium found in seawater, and solution concentrations of Ce are typically less than 10 pM,[30] it is consistent with a lack of leaching during photoprotection catalysis. Because PXRD patterns of spent and fresh antioxidant catalyst are the same, with no change in relative peak intensities of micron-size $Ce_2(CO_3)_3 \cdot 8H_2O$ (see Figure S14, Supporting Information). A similar steady state in the surface composition of Ce(III)/Ce(IV) and CO_3^{2-} (relative to total Ce) was observed in Ce 3d and C 1s XPS spectra of NTA-capped cerium carbonate nanoparticles, with used catalysts during the first 4 h of photoprotection catalysis (See Figure S3a; Supporting Information). Based on all of these data, we conclude that the formation of Ce(IV) sites during photoprotection catalysis must only occur close to the surface and not in the bulk of the cerium carbonate.

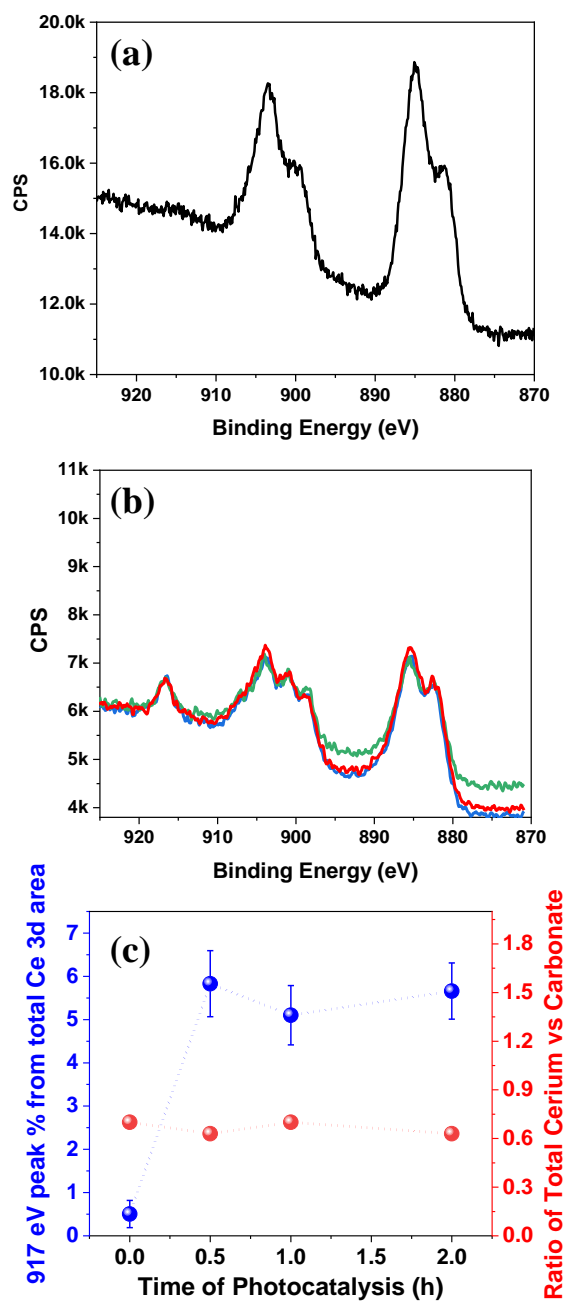**Figure 3.** (a) Ce 3d XPS spectra of micron-size $Ce_2(CO_3)_3 \cdot 8H_2O$ under tandem photoprotection catalysis conditions of Figure 2b (times in parentheses indicate duration of photoprotection catalysis): (a) control in black (0 h), and (b) used antioxidant catalyst samples in green (0.5 h),

blue (1 h), and red (2 h), (c) Steady-state value established in the ratio of total surface cerium and carbonate and in the 917 eV Ce 3d peak area versus photocatalysis time.

We combine (i) our XPS data, (ii) the well-established identity of ROS intermediates (superoxide $O_2^{\cdot-}$ and hydroxyl OH· radicals; see Figure S15, Supporting Information) in the presence of P25 TiO_2 photocatalyst under UV irradiation, and (iii) the established role of Ce(III)-enriched surface sites degrading ROS to H_2O_2 and O_2 via one-electron oxidation of Ce(III) to Ce(IV) [31] and propose a mechanism for tandem catalytic antioxidant function (see Figure S16, Supporting Information). In this mechanism, cerium carbonate catalyzes the disproportionation of photogenerated $O_2^{\cdot-}$ radicals to H_2O_2 and O_2 in the same established manner as for Ce(III)-enriched surfaces of CeO_{2-x} nanoparticles.[31] There is a second branch of the mechanism involving H_2O_2 decomposition to H_2O and O_2, which is a crude mimic of the catalase enzyme function. Two distinct sites catalyze this second branch: (i) surface Ce(IV) oxidation sites operating as thermal catalysts[32,33], and (ii) P25 TiO_2 sites operating as photocatalysts under UV irradiation.[34] In the case of the latter, H_2O_2 decomposition proceeds via a photogenerated OH· radical intermediate, which is subsequently decomposed to H_2O and O_2 via oxidation of surface Ce(III) to Ce(IV) in cerium carbonate .[31]

While the mechanism described above captures the salient features of ROS decomposition via tandem catalysis in a manner that leverages on prior literature, the actual chemistry has subtleties that are not readily elucidated based on the mechanism above, and we highlight some of these below. We investigated whether another ligand that also stabilizes Ce in the (III) valence state would lead to an equally active catalytic antioxidant. We thus investigated $CePO_4$ in the same

photoprotection catalysis experiment as shown in Figure 2 for cerium carbonate. However, we failed to observe a decrease in the MB dye photodegradation rate over background (see Figure S17, Supporting Information). We surmise that while $CePO_4$ has been previously reported to act as a photoprotection antioxidant catalyst,[35,36] it is be less active for ROS degradation than $Ce_2(CO_3)_3.6H_2O$. We also investigated the role of carbonate on its own as a further control, because there have been previous reports of carbonate anion acting as a ROS scavenger, particularly for $OH·$ radicals.[35, 36] However, Na_2CO_3 had no effect on MB dye decomposition rate via photogenerated ROS under the same conditions as used in Figure 2. We conclude that neither carbonate nor Ce(III) on their own are sufficient to account for our observations; however, when present together in cerium carbonate, a particular synergy is created between these two components, which makes them both together a more potent antioxidant than $CePO_4$ as well as cerium oxide nanoparticles (*vide supra*). This may explain the proximity that has been previously required next to the ROS emitter, when using $CePO_4$ and cerium oxide previously as photoprotection antioxidant catalysts, which has no impact when using c.[37-39]

We investigate the implications of the tandem catalysis mechanism of ROS decomposition using a comparative approach, involving degradation of MB dye in aqueous solution via photogenerated ROS intermediates using varying proportions of unpassivated rutile TiO_2 in the presence and absence of a fixed amount of micron-size $Ce_2(CO_3)_3·8H_2O$ (see Figures. S18 and S19, Supporting Information). When the TiO_2 is present without micron-size $Ce_2(CO_3)_3·8H_2O$, data in Figure 4a demonstrate a direct increase in the rate constant for MB dye photodegradation upon increasing the amount of TiO_2, consistent with its established role as an active antioxidant catalyst for MB dye degradation in solution.[40] With no added TiO_2 in Figure 4a, we still observe a significant pseudo-first-order rate constant for MB dye decomposition upon UV irradiation.

Under these conditions, the mechanism of MB dye photodegradation in aqueous solution has been established to occur through $O_2^{\cdot-}$.[41] When the same experiment is now conducted with a fixed amount (1 mg/100 mL of MB solution) of micron-size $Ce_2(CO_3)_3 \cdot 8H_2O$ and varying amounts of the rutile TiO_2, a completely different behavior is observed, as shown in Figure 4b, and we discuss these data below in parts.

First, comparing data points without the TiO_2 in Figs. 4a and 4b, the rate constant for MB dye photodegradation is 16-fold lower in the latter compared to the former. This comparison demonstrates that in the absence of added TiO_2, the initially present micron-size $Ce_2(CO_3)_3 \cdot 8H_2O$ alone must end up fulfilling the SOD and catalase functions of ROS disproportionation and H_2O_2 decomposition, respectively. We surmise that $Ce_2(CO_3)_3 \cdot 8H_2O$ must have reacted with the ROS photogenerated under these conditions and disproportionated them to produce H_2O_2 as an intermediate along with Ce(IV) sites, according to the ROS disproportionation half-cycle (see Figure S16, Supporting Information). This generated H_2O_2 must have led to the reduction of the surface Ce(IV) back to Ce(III), to release H_2O and O_2,[33] according to the H_2O_2 decomposition half-cycle (see Figure S16, Supporting Information).

Data in Figure 4b exhibit a maximum in the rate constant for MB dye degradation, at 0.25 mg of added TiO_2, and the rate constant for MB dye photodegradation decreases as the amount of rutile TiO_2 increases further in Figure 4b. This is opposite to the trend observed upon adding TiO_2 in the absence of micron-size $Ce_2(CO_3)_3 \cdot 8H_2O$, in Figure 4a. This inverse scaling of the rate constant upon TiO_2 addition in Figure 4b provides evidence of the tandem catalytic antioxidant mechanism, involving TiO_2 catalyzing the decomposition of H_2O_2 to H_2O and O_2. As the amount of TiO_2 continues to increase in Figure 4b, this latter effect of a catalase function combined with

20

the known function of TiO_2 as an ROS photogenerator (vide supra) leads to a plateau regime – where the amount of TiO_2 added has no effect on the rate constant for MB dye degradation. We observe the rate constant in this plateau regime to be 25% lower than its maximum value in Figure 4b, notwithstanding the three-fold higher amounts of TiO_2 present in the system. We stress that control experiments demonstrate that neither the presence of carbonate anions nor Ce(III) cations in combination with P25 TiO_2 are sufficient on their own for achieving tandem catalytic antioxidant function, as observed when combining P25 TiO_2 and micron-size $Ce_2(CO_3)_3 \cdot 8H_2O$ (see Figure S17, Supporting Information).[44]
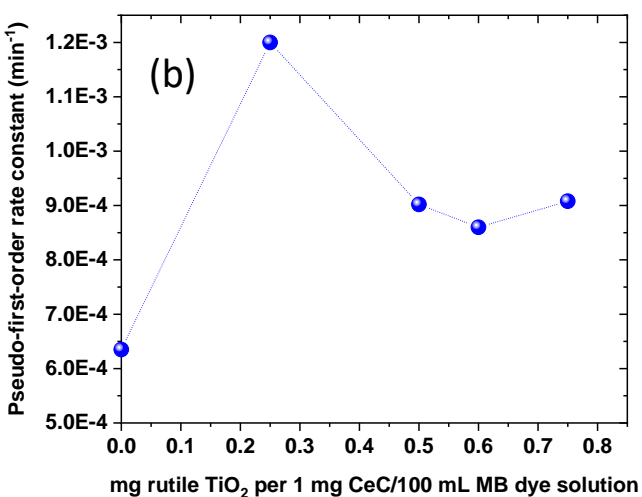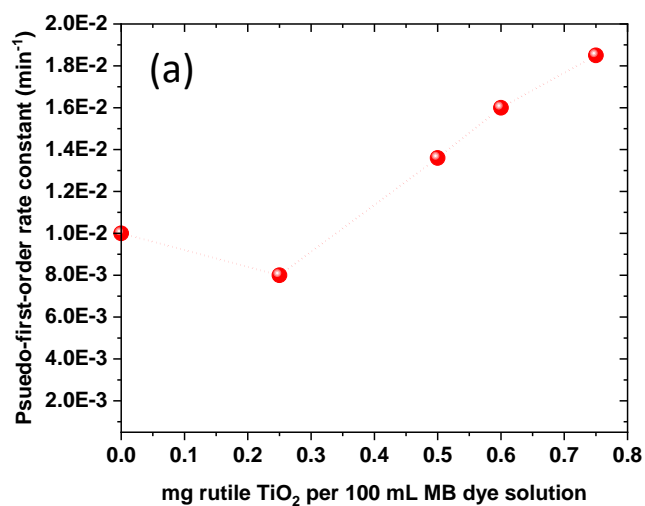
Figure 4. Plot of pseudo-first order rate constant of MB dye photodegradation in presence of varying amount of unpassivated rutile TiO_2 (average size of 300 nm) (a) in absence of added micron-size $Ce_2(CO_3)_3 \cdot 8H_2O$ and (b) in presence of added micron-size $Ce_2(CO_3)_3 \cdot 8H_2O$ (1 mg/100 mL MB dye solution).

We infer based on the data in the paragraph above that the Ce(III) and Ce(IV) surface sites present in micron-size $Ce_2(CO_3)_3 \cdot 8H_2O$ during photoprotection catalysis can themselves lead to a

tandem antioxidant catalyst for ROS decomposition, without the need for added TiO_2. This led us to investigate added micron-size $Ce_2(CO_3)_3 \cdot 8H_2O$ as a photoprotection antioxidant for polymethylmethacrylate (PMMA), also known as Plexiglass®, one of the top six polymers based on market share in the United States. PMMA is routinely used as a shatterproof and 40%-less-dense alternative to glass, for applications that require optical transparency, such as glazing and skylights.[42] However, a significant challenge when PMMA is exposed to outdoor elements comprising sunlight, water, and O_2 is its limited photostability.[43] Optical photographs demonstrate that the yellowing of the polymer otherwise observed as a result of UV irradiation can be significantly decreased with 2 wt. % of either EDTA-capped $Ce_2(CO_3)_3 \cdot 8H_2O$ or NTA-capped cerium carbonate particles dispersed within the polymer (see Figs. S20a, 20b, S21a, S21b Supporting Information), while retaining optical transparency. ATR-FTIR spectroscopic data demonstrate significantly less oxidation via polymer hydroxylation with the 2 wt. % of either EDTA-capped $Ce_2(CO_3)_3 \cdot 8H_2O$ particles or NTA-capped $Ce_2(CO_3)_3$, as evidenced by decreased intensity of bands at 3432 cm^{-1} (see Figs. S20c and S20d, S21bSupporting Information). Similar photostabilization of PMMA could also be accomplished using micron-size $Ce_2(CO_3)_3 \cdot 8H_2O$ (see Figure S22, Supporting Information). When instead commercial cerium oxide nanoparticulate photostabilizing agent (Rhodigard® W185, Solvay) was used as a drop-in additive, we observed significant yellowing of the polymer under the same conditions (see Figure S23; Supporting Information).

In an aim to further establish the generality of tandem catalytic antioxidant function offered by combinations of micron-size $Ce_2(CO_3)_3 \cdot 8H_2O$ and TiO_2, we investigated micron-size $Ce_2(CO_3)_3 \cdot 8H_2O$ (less than 1 wt. %) as a drop-in additive for acrylate-based coatings, which were formulated with either an unpassivated TiO_2 (pigment-grade rutile) or a conventional passivated TiO_2 (comprising a thin aluminosilicate coating in order to minimize photoactivity (Ti-Pure[TM] R-706)). We incorporated a uniform amount of soluble organic dye into all coatings formulations as a reporter of photodegradation resulting from 6 h of solar irradiation. For both sets of formulations, our results demonstrate significantly less (more than 4 fold effect) organic-dye photodegradation when adding $Ce_2(CO_3)_3 \cdot 8H_2O$ together with TiO_2 in the formulation, compared with coatings comprising just the corresponding TiO_2 pigment alone (see Figs. 5a versus 5b, Figs. 5c versus 5d, and Table S6, Supporting Information). In the control coatings lacking micron-size $Ce_2(CO_3)_3 \cdot 8H_2O$, we observed greater degradation with the unpassivated TiO_2 compared with the Ti-Pure[TM] R-706, which supports decreased photoactivity afforded by the passivating aluminosilicate overlayer in the latter (see Figs. 5a versus 5c and Table S6, Supporting Information). However, in stark contrast to trends for the paints lacking micron-size $Ce_2(CO_3)_3 \cdot 8H_2O$, in the coatings that combined $Ce_2(CO_3)_3 \cdot 8H_2O$ with TiO_2, we observed nearly no (less than 2%) photodegradation in the formulation comprising the unpassivated TiO_2, considerably less compared with 12% photodegradation in the one that comprised passivated TiO_2 (see Figs. 5b versus 5d and Table S6, Supporting Information). The more effective antioxidant function in the system combining micron-size $Ce_2(CO_3)_3 \cdot 8H_2O$ and unpassivated versus passivated TiO_2 pigment underscores the tandem catalytic nature of antioxidant function in the system, and further reinforces the data in Figure 4 in a paint film. We ascribe this unintuitive result to be a consequence of the more photoactive TiO_2 being a better partner for micron-size

24

$Ce_2(CO_3)_3 \cdot 8H_2O$ in catalyzing H_2O_2 intermediate decomposition, notwithstanding the unpassivated TiO_2 indeed being more active at photogenerating ROS.
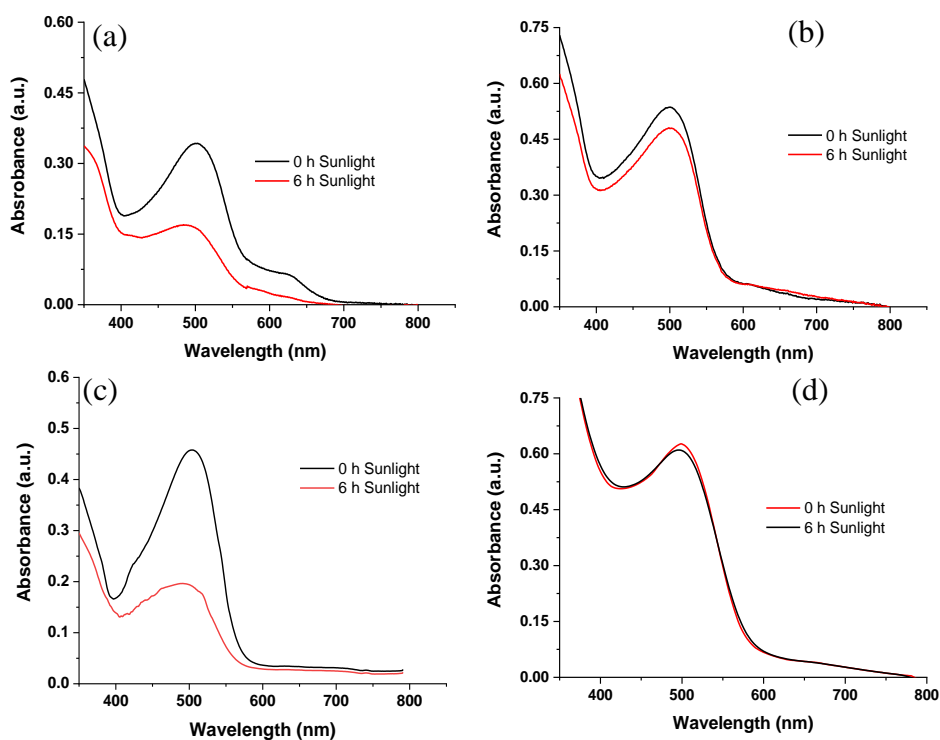
Figure 5. UV-visible spectra of CR dye extracted from sunlight irradiated paint coatings which comprise (a) Ti-Pure[TM] R-706 with no added micron-size $Ce_2(CO_3)_3 \cdot 8H_2O$, and (b) Ti-Pure[TM] R-706 with added micron-size $Ce_2(CO_3)_3 \cdot 8H_2O$ (5 wt. % relative to Ti-Pure[TM] R-706 weight). (c) UV-visible spectra of CR dye extracted from sunlight irradiated paint coatings which comprise unpassivated rutile TiO_2 and no added micron-size $Ce_2(CO_3)_3 \cdot 8H_2O$, and (d) UV-visible spectra

of CR dye extracted from sunlight irradiated paint coatings which comprise unpassivated rutile TiO$_2$ and added micron-size Ce$_2$(CO$_3$)$_3$·8H$_2$O (5 wt. % relative to the TiO$_2$ weight).

The results above motivated us to investigate EDTA-capped Ce$_2$(CO$_3$)$_3$·8H$_2$O as a drop-in additive for commercial acrylic paint formulations, which employ the same colorant pigments as real paints and coatings. A standard industrial method (ASTM D4587-11) was used to weather these paint coatings so as to reproduce damage caused by the elements, including UV irradiation, which simulates the established role of sunlight on coating color loss. Minimizing this color loss is considered to be a longstanding challenge and area of high unmet need in exterior paints and coatings. For generality, we investigated EDTA-capped Ce$_2$(CO$_3$)$_3$·8H$_2$O as a drop-in additive (4 wt. % relative to acrylic binder weight) for paints comprising three distinct commercial colorant pigments: (1) Phthalo Blue (808-7214, Colortrend®), (2) Organic Red (808-0836 Colortrend®), and (3) Red Iron Oxide (808-1045, Colortrend®). Optical photographs of the corresponding coatings before and after 4500 h of accelerated weathering are shown in Figure 6, and in all cases demonstrate significantly less visible color loss for the paints that incorporated EDTA-capped Ce$_2$(CO$_3$)$_3$·8H$_2$O as an additive. The extent of color loss was quantified with a spectrophotometer as characterized by a ΔE* value (lower ΔE* corresponds to greater color retention after weathering) and summarized in Table 2.

Table 2. Summary of QUV weathering test (ASTM D4587-11) in acrylic paint coatings.

	Phthalo Blue 808 Tinted Paint			QUV - Red Oxide Tinted Paint			QUV - Org Red Paint (4 oz/gal)		
Initial	None	EDTA capped $Ce_2(CO_3)_3 \cdot 8H_2O$	CeO_2 (Rhodigard® W185, Solvay)	None	EDTA capped $Ce_2(CO_3)_3 \cdot 8H_2O$	CeO_2 (Rhodigard® W185, Solvay)	None	EDTA capped $Ce_2(CO_3)_3 \cdot 8H_2O$	CeO_2 (Rhodigard® W185, Solvay)
L*	73.64	73.02	73.04	59.90	59.29	59.23	75.73	74.97	75.20
a*	13.50	13.63	-14.39	29.15	29.41	29.12	33.38	34.15	33.57
b*	25.64	25.94	-24.05	18.45	18.77	18.59	4.41	4.83	5.31
4500 hours									
L*	77.93	75.64	77.78	64.73	61.12	65.54	79.73	77.57	80.16
b*	-10.94	-13.06	-10.26	23.92	27.87	21.74	26.51	29.88	22.27
a*	-20.43	-22.76	-14.71	13.63	15.77	13.02	3.81	3.68	4.2
Delta E*	7.22	4.16	11.26	8.59	3.84	11.19	7.97	5.13	12.39

Optical photographs of the corresponding coatings before and after 4500 h of accelerated weathering are shown in Figure 6, and in all cases demonstrate significantly less visible color loss for the paints that incorporated EDTA-capped $Ce_2(CO_3)_3 \cdot 8H_2O$ as an additive. The extent of color loss was quantified with a spectrophotometer Supporting Informationas characterized by a ΔE* value (lower ΔE* corresponds to greater color retention after weathering) and summarized in Table 2. The three coatings with EDTA-capped $Ce_2(CO_3)_3 \cdot 8H_2O$ as a drop-in additive exhibited at least 1.6-fold to 2.9-fold higher color retention (i.e. lower ΔE* values) compared with either control coatings lacking any additive or control coatings synthesized with the same amount of cerium oxide commercial photostabilizer (Rhodigard® W185, Solvay) instead of EDTA-capped cerium carbonate (see Table S7; Figure S24, Supporting Information). We conclude that EDTA-capped cerium carbonate nanoparticles protect commercial colorants in acrylic paint formulations from

photobleaching upon weathering in a manner that cannot be achieved by cerium oxide nanoparticles under the same conditions.

We also tested color retention in paint films prepared with NTA-capped cerium carbonate, and, in this case, accelerated aging was performed by adding P25 TiO$_2$ photocatalyst to the formulation (see Figure S25, Supporting Information). Optical photographs before and after exposure to UV irradiation (365 nm) for 20 h demonstrate in a qualitative fashion much greater retention of color for the NTA-capped cerium carbonate sample compared to a control lacking any added cerium carbonate (see Figure S25, Supporting Information). These data support the same trends as observed above for the paint films comprising EDTA-capped nanoparticles above.
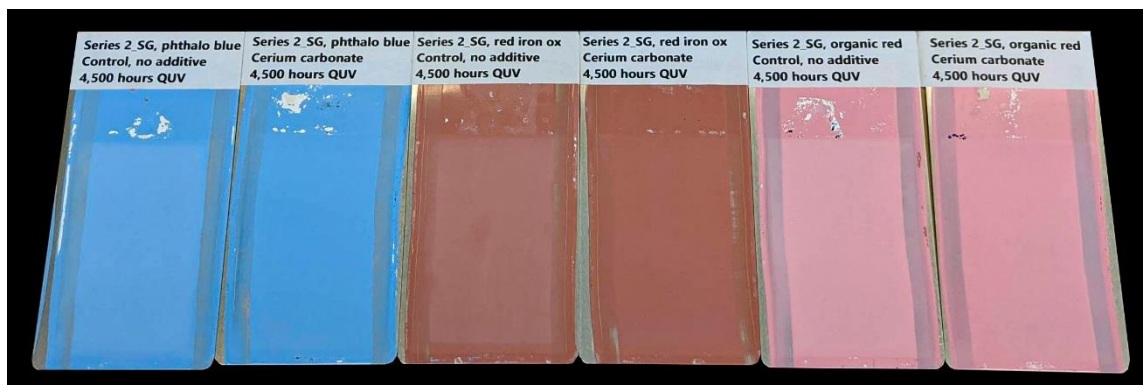

Figure 6. Photographs showing painted panels before and after accelerated weathering test via ASTM D4587-11. From left to right, the coatings comprise phthalo-blue pigment without and with EDTA-capped cerium carbonate; red iron-oxide pigment without and with EDTA-capped cerium carbonate; organic-red pigment without and with EDTA-capped cerium carbonate.

3. CONCLUSIONS

In summary, we demonstrate cerium carbonate as a robust inorganic photoprotection antioxidant, which functions effectively in tandem with conventional ROS generators consisting of photoactive metal oxides, to decompose ROS before they can degrade dye molecules, insoluble commercial organic pigments, as well as polymethylmethacrylate polymer. This catalytic antioxidant photoprotection function of cerium carbonate is significantly more active than what is observed in comparison with cerium oxide nanoparticles. It is also fully accessible in nanoparticles of cerium carbonate, which provide additional benefit to preserve the transparency of polymer films and cosmetic/aesthetic properties of paint coatings. Consistent with our XPS data on used cerium carbonate photoprotection catalysts, their mechanism crudely mimics tandem catalysis previously observed in enzymes,[17] involving reaction sequences comprising (i) ROS disproportionation to H_2O_2 (SOD function) and (ii) degradation of H_2O_2 (catalase function). However, there is a subtlety to the chemistry in that $CePO_4$ is inactive by comparison, despite the propensity of phosphate, like carbonate, to stabilize the Ce(III) valence state, and Na_2CO_3 is also inactive. These results emphasize that both Ce(III) and carbonate are crucial to the ROS degradation catalysis.

Supporting Information:
Materials and Methods
Figs. S1-S21Tables S1-S7

Acknowledgements:

References:

1. G. Fortunato, A. Rittera, D. Fabian, Old Masters' lead white pigments: investigations of paintings from the 16th to the 17th century using high precision lead isotope abundance ratios. *Analyst*, **130**, 898–906, (2005).

2. J. H. Braun, J. G. Dickinson, White Pigment. *Appl. Polym. Sci.* 483-492, (2000).

3. F. P. Gasparro, M. Mitchnick, J. F. Nash, A review of sunscreen safety and efficacy. *Photochem. Photobiol.* **68**, 243-256 (1998).

4. A. Corma, H. Garcia, Zeolite-based photocatalysts. *Chem. Commun*. 1443-1459 (2004).

5. S. Das, J. P. Ramírez, J. Gong, N. Dewangan, K. Hidajat, B. C. Gates, S. Kawi, Core–shell structured catalysts for thermocatalytic, photocatalytic, and electrocatalytic conversion of CO_2. *Chem. Soc. Rev*. **49**, 2937-3004 (2020).

6. Y-C. Chen, Y-K. Hsu, R. Popescu, D. Gerthsen, Y-G. Lin, C. Feldmann, Au@Nb@H x $K_{1-x}NbO_3$ nanopeapods with near-infrared active plasmonic hot-electron injection for water splitting. *Nat. Commun*. **9**, 232 (2018).

7. Dan-Hardi, M.; Serre, C.; Frot, T.; Rozes, L.; Maurin, G.; Sanchez, C.; Férey, G. A New Photoactive crystalline highly porous titanium(IV) dicarboxylate. *J. Am. Chem. Soc*. **131**, 10857–10859 (2009).

8. Kamegawa, T.; Shimizu, Y.; Yamashita, H. Superhydrophobic surfaces with photocatalytic self-cleaning properties by nanocomposite coating of TiO_2 and polytetrafluoroethylene. *Adv. Mater*. **24**, 3697–3700 (2012).

9. Yang, J.; Wang, D.; Han, H.; Li, C. , Roles of cocatalysts in photocatalysis and photoelectrocatalysis. *Acc. Chem. Res.* **46**, 1900–1909 (2013).

10. Mukerji, S. G.; Haick, H.; Schvartzman, M.; Paz, Y. Selective photocatalysis by means of molecular recognition. *J. Am. Chem. Soc.* **123**, 10776-10777 (2001).

11. Liu, Y.; Howarth, A. J.; Hupp, J. T.; Farha, O. K. Selective photooxidation of a mustard-gas simulant catalyzed by a porphyrinic metal–organic framework. *Angew.Chem. Int.Ed.* **54**, 9001 –9005 (2015).

12. Downs, C. A.; Fauth, J. E.; Halas, J. C.; Dustan, P.; Bemiss, J.; Oxidative stress and seasonal coral bleaching. *Free Radical Biol. Med.* **33**, 533–543, (2002).

13. Fajzulin, I.; Zhu, X.; Möller, M. Nanoparticulate inorganic UV absorbers: a review. *J. Coat. Technol. Res*. **12**, 617–632 (2015).

14. Rabek, J. F.; Ranby, B. Role of singlet oxygen in photo-oxidative degradation and photostabilization of polymers. *Polym. Eng. Sci.* **15**, 40-43 (1975).

15. Qin, B.; Cartier, L.; Dubois-Dauphin, M.; Li, B.; Serrander, L.; Krause, K-H. A key role for the microglial NADPH oxidase in APP-dependent killing of neurons. *Neurobiol Aging*. **27**, 1577–1587 (2006).

16. Harman, D.Aging: A theory based on free radical and radiation chemistry. *J. Gerontol.* **11**, 298-300 (1956).

17. Orr W. C.; Sohal, R. S. Extension of Life-Span by Overexpression of Superoxide Dismutase and Catalase in Drosophila melanogaster. *Science* **263**, 1128-1130 (1994).

18. Wang, Y. Bulky DNA Lesions Induced by Reactive Oxygen Species. *Chem. Res. Toxicol.* **21**, 276–281 (2008).

19. Lo, J. A.; Fisher, D. E. The melanoma revolution: From UV carcinogenesis to a new era in therapeutics. *Science* **346**, 945-949 (2014).

20. Mitra, D.; Luo, X.; Morgan, A.; Wang, J.; Hoang, M. P.; Lo, J.; Guerrero, C. R.; Lennerz, J. K.; Mihm, M. C.; Wargo, J. A.; Robinson, K. C.; Devi, S. P.; Vanover, J. C.; D'Orazio, J. A. ; McMahon, M.; Bosenberg, M. W.; Haigis, K. M. ; Haber, D. A.; Wang, Y. Fisher, D. E. An ultraviolet-radiation-independent pathway to melanoma carcinogenesis in the red hair/fair skin background. *Nature*, **2012,** 491, 449-453.

21. Driel, B. A. V.; Kooyman, P. J.; Berg, K. J. V.; Schmidt-Ott, A.; Dik, J. A quick assessment of the photocatalytic activity of TiO_2 pigments — From lab to conservation studio. *Microchem. J.* **2016**, 126, 162–171.

22. Record, I. R.; Dreosti, I. E.; Konstantinopoulos, M.; Buckley, R. A. The influence of topical and systemic vitamin E on ultraviolet light-induced skin damage in Hairless Mice. *Nutr. Cancer* **1991**, 16, 219-225.

23. Katiyar, S. K.; Mukhtar, H. Green tea polyphenol (−) -epigallocatechin-3-gallate treatment to mouse skin prevents UVB-induced infiltration of leukocytes, depletion of antigen-presenting cells, and oxidative stress. *J. Leukocyte Biol.* **2001**, 67, 719-726.

24. Turner, S.; Lazar, S.; Freitag, B.; Egoavil, R. ; Verbeeck, J.; Put, S.; Strauven, Y.; Van Tendeloo, G. High resolution mapping of surface reduction in ceria nanoparticles. *Nanoscale*, **2011**, 3, 3385–3390.

25. Ophus, C. Four-dimensional scanning transmission electron microscopy (4D-STEM): From scanning nanodiffraction to ptychography and beyond. *Microsc. Microanal.* **2019**, 25, 563–582.

26. Eriksson, P.; Tal, A. A.; Skallberg, A.; Brommesson, C.; Hu, Z.; Boyd, D. R.; Olovsson, W.; Fairley, N.; Abrikosov, I. A.; Zhang, X.; Uvdal, K. Cerium oxide nanoparticles with antioxidant capabilities and gadolinium integration for MRI contrast enhancement, *Sci. Rep.* **2018**, 8, 6999.

27. Ohtani, B.; Prieto-Mahaney, O. O.; Li, D.; Abe, R.; What is Degussa (Evonik) P25? crystalline composition analysis, reconstruction from isolated pure particles and photocatalytic activity test. *J. Photochem. Photobiol. A* **2010**, 216, 179–182.

28. Morlando, A.; Chaki Borrás, M.; Rehman, Y.; Bakand, S. Barker, P.; Sluyter, R.; Konstantinov, K. Development of CeO_2 nanodot encrusted TiO_2 nanoparticles with reduced photocatalytic activity and increased biocompatibility towards a human keratinocyte cell line. *J. Mater. Chem. B* **2020**, 8, 4016-4028.

29. Gao, H.; Qiao, B.; Wang, T. Wang, D.; Jin, Y.; Cerium oxide coating of titanium dioxide pigment to decrease its photocatalytic activity. *Ind. Eng. Chem. Res.* **2014**, 53, 189−197.

30. Naganuma, T.; Traversa, E.; Air, aqueous and thermal stabilities of Ce^{3+} ions in cerium oxide nanoparticle layers with substrates. *Nanoscale* **2014**, 6, 6637-6645.

31. Byrne, R. H. Inorganic speciation of dissolved elements in seawater: the influence of pH on concentration ratios. *Geochem. Trans*. **2002**, 3, 11-16

32. Xue, Y.; Luan, Q.; Yang, D.; Yao, X.; Zhou, K. Direct evidence for hydroxyl radical scavenging activity of cerium oxide nanoparticles. *J. Phys. Chem. C* **2011**, 115, 4433–4438,

33. Baldim, V.; Bedioui, F.; Mignet, N.; Margaill, I.; Berret, J.-F. The enzyme-like catalytic activity of cerium oxide nanoparticles and its dependency on Ce^{3+} surface area concentration. *Nanoscale* **2018**, 10, 6971 – 6980.

34. Xu, C.; Qu, X. Cerium oxide nanoparticle: a remarkably versatile rare earth nanomaterial for biological applications. *NPG Asia Mater.* **2014**, 6, e90.

35. Li, X.; Chen, C.; Zhao, J. Mechanism of photodecomposition of H_2O_2 on TiO_2 surfaces under visible light irradiation. *Langmuir* **2001**, 17, 4118-4122.

36. Joshi, A. A.; Locke, B. R.; Arce, P.; Finney, W. C. Formation of hydroxyl radicals, hydrogen peroxide and aqueous electrons by pulsed streamer corona discharge in aqueous solution. *J. Hazard. Mater.* **1995**, 41, 3-30.

37. Vieira, G. B.; José, H. J.; Peterson, M.; Baldissarelli, V. Z.; Alvarez, P.; Fátima Peralta Muniz Moreira, R. CeO_2/TiO_2 nanostructures enhance adsorption and photocatalytic degradation of organic compounds in aqueous suspension. *J. Photochem. Photobiol. A* **2018**, 353, 325-336.

38. Yang, H.; Mao, J.; Properties of $AlPO_4/CePO_4$ hybrid coating on rutile TiO_2*, Surf. Eng.* **2017**, 33, 226-230.

39. Guo, H.; Klose, D.; Hou, Y.; Jeschke, G.; Burgert, I. Highly Efficient UV Protection of the Biomaterial Wood by A Transparent TiO_2/Ce Xerogel, *ACS Appl. Mater. Interfaces*, **2017**, 9, 39040−39047.

40. Titanium dioxide pigment coated with cerium cations, selected acid anions, and alumina*, U. S. Patent* 4,737,194 , 1988..

41. Mishra, M. K.; Chattopadhyay, S.; De, G. Low Temperature Fabrication of Photoactive Anatase TiO_2 Coating and Phosphor from Water–Alcohol Dispersible Nanopowder. *Ind. Eng. Chem. Res.* **2015**, 54, 928–937.

42. Nassar, S. J. M.; Wills, C.; Harriman, A. Inhibition of the Photobleaching of Methylene Blue by Association with Urea. *ChemPhotoChem* **2019**, 3, 1042–1049.

43. Novak, R. W.; Lesko, P. M. "Methacrylic Polymers" in *Kirk-Othmer Encyclopedia of Chemical Technology*, Ed. Kirk-Othmer, Wiley, **2000**.

44. Enko, B.; Borisov, S. M.; Regensburger, J.; Bäumler, W.; Gescheidt, G.; Klimant, I. Singlet oxygen-induced photodegradation of the polymers and dyes in optical sensing materials and the effect of stabilizers on these processes. *J. Phys. Chem. A* **2013**, 117, 8873–8882.